

Volcano Trend in Electrocatalytic CO₂ Reduction Activity over Atomically Dispersed Metal Sites on Nitrogen-Doped Carbon

Jingkun Li,[†] Paulina Pršlja,[‡] Tatsuya Shinagawa,^{§,∇} Antonio José Martín Fernández,[§] Frank Krumeich,^{||} Kateryna Artyushkova,[⊥] Plamen Atanassov,[#] Andrea Zitolo,^{||} Yecheng Zhou,[‡] Rodrigo García-Muelas,[‡] Núria López,[‡] Javier Pérez-Ramírez,[§] and Frédéric Jaouen^{*,†}

[†]Institut Charles Gerhardt Montpellier, UMR 5253, CNRS, Université Montpellier, ENSCM, Place Eugène Bataillon, 34095 Montpellier Cedex 5, France

[‡]Institute of Chemical Research of Catalonia, ICIQ, The Barcelona Institute of Science and Technology, Av. Països Catalans, 16, 43007 Tarragona, Spain

[§]Institute for Chemical and Bioengineering, Department of Chemistry and Applied Biosciences and ^{||}Laboratory of Inorganic Chemistry, Department of Materials, ETH Zurich, Vladimir-Prelog-Weg 1, 8093 Zurich, Switzerland

[⊥]The Department of Chemical and Biological Engineering, Center for Micro-Engineered Materials (CMEM), University of New Mexico, Albuquerque, New Mexico 87131, United States

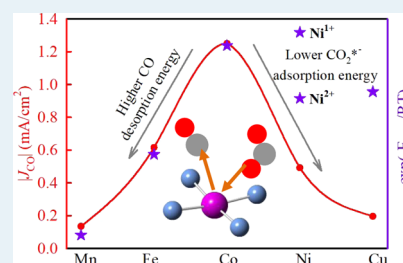
[#]Chemical and Biomolecular Engineering, University of California Irvine, Irvine, California 92697, United States

[∇]Synchrotron SOLEIL, L'Orme des Merisiers, BP 48 Saint Aubin, 91192 Gif-sur-Yvette, France

Supporting Information

ABSTRACT: The development of catalysts for electrochemical reduction of carbon dioxide (eCO₂RR) with high activity and selectivity remains a grand challenge to render the technology useable. As promising candidates, metal–nitrogen–carbon (MNC) catalysts with metal atoms present as atomically dispersed metal–N_x moieties (MN_x, M = Mn, Fe, Co, Ni, and Cu) were investigated as model catalysts. The distinct activity for CO formation observed along the series of catalysts is attributed to the nature of the transition metal in MN_x moieties because of otherwise similar composition, structure, and morphology of the carbon matrix. We identify a volcano trend between their activity toward CO formation and the nature of the transition metal in MN_x sites, with Fe and/or Co at the top of the volcano, depending on the electrochemical potential. Regarding selectivity, FeNC, NiNC, and MnNC had Faradaic efficiency for CO >80%. To correctly model the active sites in operando conditions, experimental operando X-ray absorption near edge structure spectroscopy was performed to follow changes in the metal oxidation state with electrochemical potential. Co and Mn did not change the oxidation state with potential, whereas Fe and Ni were partially reduced and Cu largely reduced to Cu(0). Computational models then led to the identification of M²⁺N₄–H₂O as the most active centers in FeNC and CoNC, whereas Ni¹⁺N₄ was predicted as the most active one in NiNC at the considered potentials of –0.5 and –0.6 V versus the reversible hydrogen electrode. The experimental activity and selectivity could be rationalized from our density functional theory results, identifying in particular the difference between the binding energies for CO₂*[–] and H* as a descriptor of selectivity toward CO. This in-depth understanding of the activity and selectivity based on the speciation of the metals for eCO₂RR over atomically dispersed MN_x sites provides guidelines for the rational design of MNC catalysts toward eCO₂RR for their application in high-performance devices.

KEYWORDS: CO₂ electroreduction, CO₂ activation, MNC catalyst, single-atom catalyst, metal–N₄ electrocatalysis



1. INTRODUCTION

Global climate change triggered by anthropogenic emission of CO₂ is a growing threat to society. Direct electrochemical reduction of CO₂ (eCO₂RR) to produce value-added chemicals and fuels using renewable electricity is a promising strategy for closing the carbon cycle. However, this early-stage technology is challenged by the low activity and selectivity because of the extremely stable C=O bond (806 kJ mol^{–1}) in CO₂ and the competing hydrogen evolution reaction (HER) in aqueous electrolytes.^{1,2} Thus, it is of paramount importance to

identify robust catalysts with economically viable current density at low overpotential and high selectivity toward eCO₂RR.

Large ensembles of crystallographically ordered metal atoms (reduced metals, metal-oxides, chalcogenides, metal-oxide@metal core@shell, etc.) have hitherto been the most studied

family of eCO₂RR catalytic sites. They can be categorized into four types, according to their main eCO₂RR products and/or selectivity:^{3–5} (1) formate or formic acid for catalytic sites with low binding energy for CO₂* (typical examples are ensembles based on Sn or Pb); (2) CO for catalytic sites with strong COOH* binding but weak CO* binding (typical examples are metallic surfaces such as Au, Ag); (3) products corresponding to 4–12 electron reduction (HCHO, CH₃OH, CH₄, C₂H₄, C₂H₅OH) for catalytic sites with less weak CO* binding energy (metallic Cu is an outstanding material for achieving this); (4) catalytic sites with low selectivity toward eCO₂RR, with H₂ as the main product (such as Pt or Ni metallic surfaces).

A second family of eCO₂RR catalysts involves active sites based on a single metal-atom coordinated only with nonmetal elements. In this family, the subgroup of molecular catalysts with a well-defined metal coordination have been studied since the 1970s and have shown promising properties for eCO₂RR.⁵ In particular, some transition-metal phthalocyanines and porphyrins with well-defined square-planar MN₄ structure presented high selectivity toward CO formation.^{6–9} The electroreduction of CO₂ to CO (CO₂ + 2H⁺ + 2e⁻ → CO + H₂O) with standard electrochemical potential of -0.11 V versus a reversible hydrogen electrode (RHE) is attractive as it requires the transfer of only two electrons, leading to lower activation barriers than for hydrocarbon formation.⁴ Together with formic acid, CO has thus been identified as the economically most appealing product of eCO₂RR.^{2,4} Moreover, the simultaneous production of CO and H₂ (syngas) in appropriate composition during eCO₂RR on surfaces with multiple catalytic sites may be used to prepare synthetic fuels via a downstream Fischer–Tropsch process.¹⁰ Molecular catalysts however have several disadvantages, such as cost related to their synthesis, lower operando stability because of metal leaching or chemical degradation, and poor electrical connection with the conductive support, impeding reaching high current densities in a CO₂/water electrolyzer.^{11,12}

As a second subgroup of catalysts with single metal-atom sites for eCO₂RR, metal–nitrogen–carbon (MNC) materials exclusively comprising atomically dispersed transition-metal cations covalently bonded with nitrogen atoms (MN_x moieties) hold promise to overcome the above disadvantages of molecular catalysts while retaining high activity and selectivity toward CO formation.^{13–21} The metal-ion coordination in MNC materials resembles the local patterns existing in metal–N₄ macrocycles. Such materials were initially developed for catalyzing the oxygen reduction reaction (ORR), in particular in acidic medium, with focus on the FeN_x and CoN_x as other MN_x motives have a much lower ORR activity.^{22–25} MNC materials are prepared via the self-assembly of metal, nitrogen, and carbon atoms at a high temperature. However, the elevated temperature and excess of metal often lead to the formation of clusters of metal atoms (metallic, metal-oxide, metal-carbide, etc.) along with the MN_x sites.^{26–28} This has for a long time impeded the elucidation of the MN_x site structures and their ORR catalytic activities.²⁵ In the context of eCO₂RR, the presence of metal clusters along with MN_x moieties may, depending on the nature of the metal, catalyze the HER^{10,29–31} and/or other pathways of eCO₂RR. This has prevented establishing clear experimental structure-to-property relationships between the nature of the metal in MN_x and their activity and selectivity toward eCO₂RR. In addition, the presence of even a minute amount of metallic

clusters in MNC catalysts also impedes a reliable comparison between experimental eCO₂RR activity/selectivity trends for such materials and density functional theory (DFT) results obtained on MN₄ sites.^{32–34} Validation of DFT predictions on a reasonably large series of model materials is highly important to speed up the rational identification of more promising MNC candidates for eCO₂RR,² given that the library of metals demonstrated to form MN_x sites in carbon has been recently expanded also to heavier elements such as Sn,³⁵ Ru,³⁶ Pt,³⁷ Pd,³⁷ and so on. The investigation of model MNC catalysts exclusively comprising atomically dispersed MN_x sites is thus critical to understand their structure–performance relationships and to identify the proper activity/selectivity descriptor(s). Whereas numerous studies have now reported the eCO₂RR selectivity of some atomically dispersed MNC catalysts prepared by different synthetic approaches,^{13,16,20,38} a single study has, to the best of our knowledge, compared the trends in activity and selectivity for a narrow family of three atomically dispersed MNC catalysts prepared identically except for the nature of the metal element.²¹ The synthesis leaned toward silica templating of *o*-phenylenediamine and Fe, Co, or Ni salts. Whereas metal particles formed in parallel to MN_x sites during the first pyrolysis, they could be removed during subsequent NaOH etching and acid-wash steps. However, the formation of metallic particles during the first pyrolysis leads to markedly different pore size distributions, in particular for CoNC. This rendered the comparison of the materials more complex because of expectedly different utilizations of the MN_x sites for different pore size distributions.

Herein, we applied a robust synthesis approach involving a sacrificial Zn-based metal–organic framework (MOF) and a metal salt (Mn, Fe, Co, Ni, or Cu) that resulted in the complete integration of the metal atoms as atomically dispersed MN_x moieties in the N-doped carbon matrix derived from the MOF, without formation of metallic particles. With this series of five model MNC catalysts, a volcano trend in their catalytic activity toward CO₂ electroreduction to CO could be revealed for the first time, with the CoN₄ moieties exhibiting the highest intrinsic activity at -0.6 V versus RHE. Our operando spectroscopy characterization and DFT models further reveal the importance of the speciation of the metal center under reaction conditions in order to correctly interpret and predict the competition between CO₂ activation, CO and H adsorption, thus providing a more accurate understanding of the activity of eCO₂RR toward CO over MN_x motives.

2. EXPERIMENTAL METHODS

2.1. Catalyst Synthesis. All catalyst precursors were prepared via dry ball-milling of the Zn(II) zeolitic imidazolate framework (Basolite Z1200 from BASF, labeled ZIF-8), M²⁺ acetate (M = Mn, Fe, Co, Ni, and Cu), and 1,10-phenanthroline. 1,10-phenanthroline (200 mg), 800 mg of ZIF-8, and a certain amount of M²⁺ acetate corresponding to 0.5 wt % transition metal in the total precursor were weighed and poured into a ZrO₂ crucible with 100 zirconium-oxide balls of 5 mm diameter. The ZrO₂ crucible was then sealed under air and placed in a planetary ball-miller (Fritsch Pulverisette 7 Premium, Fritsch, Idar-Oberstein, Germany). The powders were milled for four cycles of 30 min at 400 rpm milling speed. The catalyst precursors resulting from the milling were pyrolyzed at 1050 °C in Ar for 1 h. The obtained catalysts were labeled MNC. A control sample was also

synthesized according to this process, except that no separate metal acetate was added (labeled (Zn)NC).

2.2. Scanning Transmission Electron Microscopy. For the scanning transmission electron microscopy (STEM) investigations, the material was dispersed in ethanol and a few drops of the suspension deposited onto a perforated carbon foil supported on a copper grid. After evaporation of the ethanol, the grid was mounted on the single tilt holder of the microscope. STEM images were recorded on an aberration-corrected HD2700CS (Hitachi) with a high-angle annular dark-field detector (HAADF). CuNC was measured on a Mo grid to avoid the Cu stray radiation from the TEM grid. STEM combined with energy-dispersive X-ray (EDX) spectroscopy was performed on a Talos F200X microscope (ThermoFisher) with a high brightness field emission gun operated at an acceleration potential of 200 kV. The EDX system of this microscope consists of four silicon drift detectors, which enables one to record EDX maps with good signal to noise ratio in a relatively short collection time (here 10–20 min).

2.3. X-ray Diffraction. X-ray diffraction (XRD) patterns were obtained using a PANalytical X'Pert Pro powder X-ray diffractometer with Cu K α radiation.

2.4. X-ray Absorption Spectroscopy. Metal K-edge X-ray absorption spectroscopy (XAS) was conducted at room temperature at SAMBA beamline (Synchrotron SOLEIL). The beamline is equipped with a sagittally focusing Si 220 monochromator and two Pd-coated mirrors that were used to remove X-rays harmonics. The catalysts were pelletized as disks of 10 mm diameter with 1 mm thickness using Teflon powder (1 μ m particle size) as a binder. The detailed analysis method for the extended X-ray absorption fine structure (EXAFS) data can be found elsewhere.^{24,25}

For operando XAS measurements, catalyst inks were prepared by mixing 10 mg of catalyst with 50 μ L of deionized water and 100 μ L of 5 wt % Nafion solution with ultrasound. A 50 μ L aliquot was then pipetted on a \sim 3 cm² circular area of a 100 μ m thick graphite foil (Goodfellow cat. C 000200/2), resulting in a catalyst loading of \sim 1 mg cm⁻². The graphite foil then served as a working electrode, and was installed in an electrochemical cell²⁴ (PECC2, from Zahner) with an Ag/AgCl (saturated KCl) reference electrode, a Pt counter electrode, and CO₂-saturated 0.1 M KHCO₃ electrolyte. Operando measurements were performed by recording the K α X-ray fluorescence of Fe with a Canberra 35-elements monolithic planar Ge pixel array detector.

2.5. X-ray Photoelectron Spectroscopy. X-ray photoelectron spectroscopy (XPS) spectra were acquired on a Kratos Axis DLD Ultra-X-ray photoelectron spectrometer using an Al K α source monochromatic operating at 150 W with no charge compensation. The base pressure was about 2×10^{-10} Torr and the operating pressure was around 2×10^{-9} Torr. Survey and high-resolution spectra were obtained at pass energies of 80 and 20 eV, respectively. Acquisition times were 2 min for survey spectra, 3 min for C 1s spectra, and 40 min for N 1s and M 2p spectra. Data analysis and quantification were performed using CasaXPS software. A linear background subtraction was used for quantification of C 1s, O 1s, and N 1s spectra, whereas a Shirley background was applied to the M 2p spectra. Sensitivity factors provided by the manufacturer were utilized to obtain atomic percentages of Fe, N, C, and O present in samples, and the elemental percentage reported was the average of five spots per sample. A 70% Gaussian/30%

Lorentzian line shape was utilized in the curve fitting. Averages from three areas per sample were presented. N 1s spectra were fitted with a set of components with a fixed energy position, in accordance with a previous study.³⁹ The fitting components are assigned to pyridinic N (398.8 eV), N in MN_x moieties (398.8–399.9 eV), pyrrolic and hydrogenated N (400.7 eV), graphitic N (401.8 and 402.7 eV), and N-oxide (404.3 and 405.6 eV).

2.6. Scanning Electron Microscopy. Scanning electron microscopy (SEM) micrographs were obtained with a Hitachi S-4800 apparatus (Hitachi, Tokyo, Japan).

2.7. N₂ Physisorption. N₂ physisorption analysis was performed at liquid nitrogen temperature (77 K) with a Micromeritics ASAP 2020 instrument. Prior to the measurements, MNC materials were degassed at 200 °C for 5 h in flowing nitrogen to remove guest molecules or moisture.

2.8. Raman Spectroscopy. Raman spectra were collected using a LabRAM ARAMIS Raman microscope with a 473 nm laser.

2.9. Linear Scan Voltammetry. Catalyst powders were deposited on glassy carbon as the working electrode. Catalyst inks were prepared by dispersing 10 mg of catalyst in a mixture of Millipore water (36.5 μ L, 18.2 M Ω cm) and ethanol (300 μ L, Sigma-Aldrich, 99.8%), into which 5 wt % Nafion solution (108.5 μ L, Sigma-Aldrich) was added as a binder. The ink was sonicated for 60 min, and an aliquot of 7 μ L was dropcast onto glassy carbon (0.196 cm², Pine instrument), to reach 800 μ g cm⁻² loading. The resulting working electrode was used in a three-electrode cell setup connected to a bipotentiostat (Biologic SP 300) and rotator (Pine Instruments). A graphite rod and Ag/AgCl (saturated KCl) were used as counter and reference electrodes, respectively. eCO₂RR activity was measured in CO₂-saturated 0.1 M KHCO₃ (pH = 6.7), and a 0.1 M N₂-saturated KH₂PO₄/K₂HPO₄ buffer solution (pH = 6.7) was used as CO₂-free blank. Linear scan voltammetry (LSV) was carried out from -0.6 to -1.4 V versus Ag/AgCl with a scan rate of 5 mV s⁻¹ at 1600 rpm. The change of potential scale versus RHE was done according to the following equation

$$\begin{aligned} E(\text{V vs RHE}) &= E(\text{V vs Ag/AgCl}) \\ &+ E(\text{V of Ag/AgCl vs NHE}) \\ &+ 0.059 \times \text{pH} \end{aligned} \quad (1)$$

where E (V of Ag/AgCl vs NHE) = 0.199 V.

2.10. Chronoamperometry and Product Analysis. Catalysts were deposited on carbon gas diffusion layers (GDLs) by airbrushing. The ink was prepared by dispersing 50 mg of catalyst powder in a mixture of Millipore water (4 mL, 18.2 M Ω cm) and 2-propanol (4 mL, Sigma-Aldrich, 99.8%), into which 5 wt % Nafion solution (50 μ L, Sigma-Aldrich) was added as a binder. The ink was sonicated for 15 min, and then sprayed onto the GDL (Sigracet 39BC, SGL Group) with an airbrush (Iwata Eclipse HP-SBS) at 353 K. The loading was 0.64 mg cm⁻² in average, with a standard deviation of 0.03 for all prepared electrodes.

A custom gas-tight glass cell with two compartments separated by a Nafion 212 membrane (Alfa Aesar, 0.05 mm thickness) was employed for the electrochemical study. Both catholyte and anolyte chambers were filled with 40 cm³ of a 0.1 M KHCO₃ solution (Sigma-Aldrich, 99.95% trace metals basis) prepared with ultrapure water. Before (20 min) and

during the measurement, CO₂ (Messer, purity 4.8) was supplied to the catholyte at a flow rate of 20 cm³ min⁻¹, resulting in a pH level of 6.7. A Pt wire and an Ag/AgCl (3.0 M KCl) electrode were used as counter and reference electrodes, respectively. The geometric surface area of the working electrodes was in the range of 1–6 cm², accurately quantified for each electrode with the ImageJ image processing and analysis software (Wayne Rasband, National Institutes of Health). All measurements were performed using an Autolab PGSTAT302N potentiostat at room temperature. The double layer capacitance of the electrodes was assessed by cyclic voltammetry (CV) at varying scan rates in the potential range of open circuit potential (OCP) ±15 mV and performing a linear fit only in the region of scan rates where a straight line between electric charge and scan rate is observed. The performance of the prepared electrodes for eCO₂RR was investigated by chronoamperometry (CA) at -0.5 and -0.6 V versus RHE for 1.5 h. These potentials were chosen because they result in sufficient currents to quantify the formed eCO₂RR products with high precision while at the same time avoiding excessive Faradaic reduction currents, which would otherwise lead to mass-transport limitations and local pH changes, implying that the measured current would not only be controlled by electrochemical kinetics but by other factors as well.⁴⁰ CAs were performed with the *iR* compensation function set at 85% of the uncompensated resistance (*R_u*), which was determined before the start of the CAs and updated every 10 min by potentiostatic electrochemical impedance spectroscopy at the electrolysis potential (100 kHz, 10 mV amplitude). The remaining 15% of the *iR* loss was corrected manually by the *R_u* measured by the impedance spectroscopy. Current densities were normalized by the geometric surface area.

Gaseous products were analyzed using an on-line gas chromatograph (SRI 8610C, Multi-Gas #3 configuration) with Ar as a carrier gas, which was equipped with a HayeSep D column and a Molecular Sieve 13X column. Gas samples were injected through a sampling loop and analyzed 10 min after the start of the electrolysis and thereafter every 15 min. The Faradaic efficiency (FE) for the gaseous products was calculated with the following equation

$$\text{FE} = \frac{\text{gas flow through the cell} \times \text{concentration of the product}}{\text{electric current at sampling time}/nF} \times 100 \quad (2)$$

Liquid products were examined with a high-performance liquid chromatograph in a Merck LaChrom system equipped with a Bio-Rad Aminex HPX-87H column heated at 333 K and a refractive index detector (Hitachi Chromaster 5450), using 5 mM H₂SO₄ as eluent. The FE for the liquid products was quantified by analyzing the catholyte after the test using the following equation

$$\text{FE} = \frac{\text{catholyte volume} \times \text{concentration of the product}}{\text{total charge passed during the electrolysis}/nF} \times 100 \quad (3)$$

In the above equations, *n* is the number of electrons transferred and *F* is the Faraday constant.

2.11. Computational Details. All calculations were performed using spin-polarized DFT as implemented in the Vienna Ab initio Simulation Package (VASP).^{41,42} The GGA

PBE-D3 was the functional of choice.^{43,44} Core electrons were described by the projector augmented wave,^{42,45} and valence electrons were expanded by plane wave basis sets with a kinetic energy cut-off of 500 eV. To model atomically dispersed metal–N_{*x*} carbon structures, we used graphene layer expanded in a (6 × 6) supercell replacing four C atoms by nitrogens and removing two C atoms to compensate for the valence. These layers were interleaved by 12 Å vacuum along the *z* direction. Various transition metal atoms (*M* = Mn, Fe, Co, Ni, Cu, Zn) were placed in the cavity left on the carbon sheet. In this configuration, two axial positions are empty. However, most of these atoms prefer octahedral coordinations,⁴⁶ and thus water-derived ligands (*L* = none, H₂O, OH, O) typically occupy one of the axial positions in aqueous electrolytes. The empty coordination site is then employed to investigate the competitive eCO₂RR and HER. Structures were relaxed with a force threshold of 0.05 eV/Å. The Brillouin zone was sampled using a 3 × 3 × 1 *k*-point mesh generated with the Monkhorst–Pack method.⁴⁷ To obtain the energies of the relevant intermediates in the electrochemical environment, the computational hydrogen electrode (CHE) was used.^{48,49} The speciation of the different oxidation states of the metals in the carbon lattice was performed via a Pourbaix diagram derived with Phonopy.⁵⁰ The optimized structures can be retrieved from ioChem-BD.^{51,52}

3. RESULTS

3.1. Structural Characterization of Pristine Catalysts.

Leaning on the synthetic route developed by our group for the preparation of FeNC and CoNC materials that exclusively comprise MN_{*x*} moieties,^{24,25} we expanded it to prepare MnNC, NiNC, and CuNC materials. A control sample was synthesized by the same approach without the addition of divalent metal acetate, and was labeled (Zn)NC, with (Zn) indicating the possible presence of residual Zn from ZIF-8, as discussed later. The MNC materials were first characterized by HAADF-STEM. Multiple areas of the samples were examined, and no metallic particles could be observed (Figure 1). The absence of crystalline metallic species in as-prepared MNC materials was further confirmed by powder XRD (Figure S1), exhibiting only two broad reflection peaks typical for nanometric graphite-like domains present in amorphous N-doped carbon materials. Elemental mapping with EDX spectroscopy showed a homogenous distribution of the metal, C and N atoms in the catalysts, revealing also the presence of residual Zn from ZIF-8 in all five MNC catalysts (Figure S2). These STEM and EDX analyses indicate that the metals are probably atomically dispersed in the nitrogen-doped carbon matrix. However, because of limited resolution of the EDX mapping, nano- or sub-nano-sized metal clusters cannot be excluded at this stage.

In order to unambiguously demonstrate the absence of metal clusters and to identify the metal coordination and bond distances in atomically dispersed MN_{*x*} sites, we resorted to EXAFS spectroscopy (Figure 2). The Fourier transform (FT) of the ex situ EXAFS spectra [*κ*² weighted *χ(κ)*] of all MNC catalysts at their respective metal K-edge energy exhibited a major peak at ~1.5 Å, attributed to the backscattering by light atoms (C, N, or O) situated in the first coordination shell of the absorbing metal. The secondary peak(s) at 2–3 Å is associated with the contribution of carbon (or N, O) atoms in the second coordination sphere of the metal center. The FT-EXAFS spectra of the MNC catalysts agree well with those of

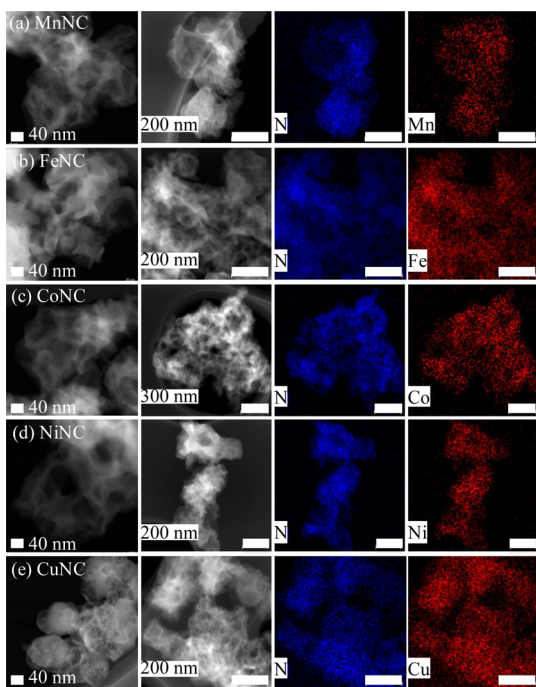


Figure 1. MNC catalyst morphology: high-resolution TEM characterization. TEM images and EDX elemental mappings for N and the respective metal derived from the metal-acetate precursor of (a) MnNC, (b) FeNC, (c) CoNC, (d) NiNC, and (e) CuNC.

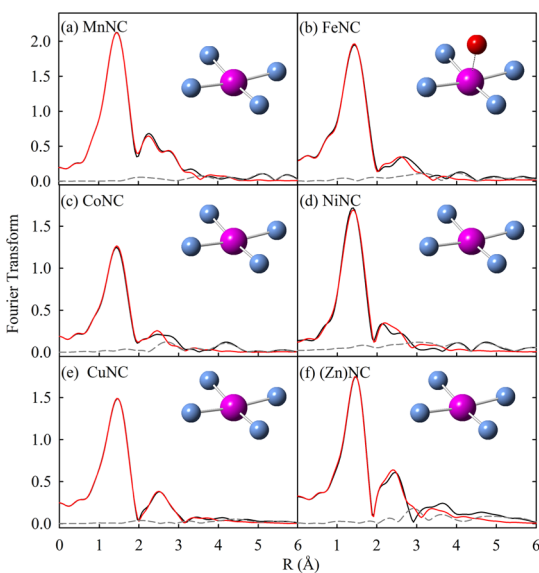


Figure 2. Atomically dispersed MN_x sites: metal K-edge EXAFS analysis. (a) MnNC, (b) FeNC, (c) CoNC, (d) NiNC, (e) CuNC, and (f) (Zn)NC. The black curves represent the experimental spectra, whereas the red curves represent calculated spectra based on the depicted structures. The dashed gray curves are the difference between experimental and calculated spectra. Metal, nitrogen, and oxygen atoms are represented in purple, blue, and red, respectively (carbon atoms in the second coordination sphere are not shown). No phase-shift correction was applied to the FTs.

some atomically dispersed MNC materials previously reported by other groups.^{13,20}

The metal K-edge EXAFS spectra were then fitted with the model structures depicted in the insets of Figure 2. For CoNC, NiNC, and CuNC, a variable number of in-plane nitrogen

atoms binding the metal–cation center were allowed for the fitting, while the spectra of FeNC and MnNC were fitted assuming the presence of four in-plane nitrogen atoms, and either one or two oxygen atoms as axial ligands. This approach was used to reduce the number of EXAFS parameters in the fit, as FeN_x and MnN_x moieties have a higher affinity to oxygen compared to other metal– N_4 moieties.⁵³ The structural parameters obtained from the fittings are shown in Table 1, including the coordination number (CN) and M–N bond distances. The best-fit results show a CN-value of ~ 4 for MnNC, CoNC, NiNC, and CuNC, suggesting that the vast majority of metal cations in these catalysts could be involved in MN_4 moieties. EXAFS alone however cannot distinguish between N, C, and O atoms, which means that the CN value of 4 may also be acceptable, from a structural viewpoint, with a mix of N, C, and O atoms. From a chemical viewpoint however, metal–nitrogen bonds in the first coordination sphere are more likely than metal–carbon or metal–oxygen ones. For Fe and Co, time-of-flight secondary-ion mass spectroscopy revealed the major presence of $MN_2C_y^+$, $MN_4C_y^+$.⁵⁴ Experimentally, it has also been shown that nitrogen is critical for the formation of single Fe atom site in a carbon support during pyrolysis, only metallic Fe particles being observed in the absence of nitrogen in the synthesis.⁵⁵ For other metals of the 3d row, although less experimental characterization has been reported yet, DFT predicts higher energy stability for metal– N_4 defects in graphene than metal– C_4 defects.⁵⁶ For those reasons, we started by investigating in-plane MN_4 sites in our DFT study to explain the reactivity, as reported in Section 4.2. With the starting hypothesis of the in-plane FeN_4 site, the higher average CN-value of 5–6 for FeNC^{22,25} strongly suggests that one or two axial O atoms are adsorbed on top of FeN_4 moieties, resulting in coordinatively saturated iron cations, in line with the high oxophilicity of Fe.

It should be noted that ZnN_x moieties with an average CN of ~ 4 are present not only in the control sample (Zn)NC (Figure 2f and Table 1) but also in all five MNC samples. The Zn K-edge X-ray absorption near edge structure (XANES) and EXAFS spectra of the five samples are identical to that recorded for (Zn)NC (Figure S3), implying that the ZnN_x coordination is unaffected by the presence of a second metal. The coexistence of ZnN_x and MN_x moieties is another indication that the metal content (from metal acetate) is not saturating the material, explaining the absence of metallic particles. In summary, the EXAFS spectra were fitted with in-plane MN_4 structures, with an axial oxygen atom needed to obtain a best-fit only for FeNC. Most important, no M–M backscattering signal was needed to get an excellent EXAFS fit, unambiguously indicating the isolated nature of the metal centers.

The metal–nitrogen bond distance and K-edge EXAFS spectra were also calculated ab initio for MN_4C_{10} model sites (10 in-plane carbon atoms in the second coordination sphere) in graphene sheets, with or without axial oxygen adsorbates (Figure S4). Considering water as an oxygen ligand, MnN_4 (2.40 Å), FeN_4 (2.33 Å), CoN_4 (2.31 Å), and ZnN_4 (2.35 Å) exhibited similar M–O bond distance between 2.31 and 2.40 Å (Table S1). No water could be stabilized on the CuN_4 and NiN_4 models. The DFT-calculated EXAFS spectra shown in Figure S5 have characteristic features analogous to those of the experimental FT-EXAFS spectra in Figure 2 with a main peak assigned to N or O back-scattering from the first coordination sphere. The calculated and experimental M–N distances are

Table 1. Structural Parameters Obtained from the Analysis with MN_x Moieties of the Metal K-Edge EXAFS Spectra and DFT Calculations^a

	MnNC	FeNC	CoNC	NiNC	CuNC	(Zn)NC
R_{M-N} (Å)	1.89(1)	1.99(2)/2.01(2)	1.96(2)	1.92(1)	1.94(1)	2.00(1)
σ^2 (Å ²)	0.0033(4)	0.008(2)	0.008(2)	0.007(1)	0.0072(7)	0.0056(3)
CN	4	5/6	3.8(6)	4.3(3)	3.9(3)	4.1(4)
R_{M-N}^* (Å)	1.91	1.89	1.89	1.88	1.93	1.96

^a R_{M-N} is the metal–nitrogen bond distance, σ^2 the Debye–Waller factor, and CN the coordination number, obtained from EXAFS fitting, whereas R_{M-N}^* is the DFT simulated metal–nitrogen bond distance for MN_4C_{10} model sites. Errors are given in brackets, for example, 1.89(1) means 1.88–1.90.

also in good agreement, except for Fe, for which the EXAFS fitting is complicated by the presence of axial oxygen ligands (Tables 1 and S1).

The oxidation state of the atomically dispersed metal centers was then investigated with XPS. No signal related to metal(0) state could be observed in the M 2p spectra. The narrow-scan spectra in the binding energy regions corresponding to the M 2p_{3/2} spin–orbit couplings are shown in Figure 3. They

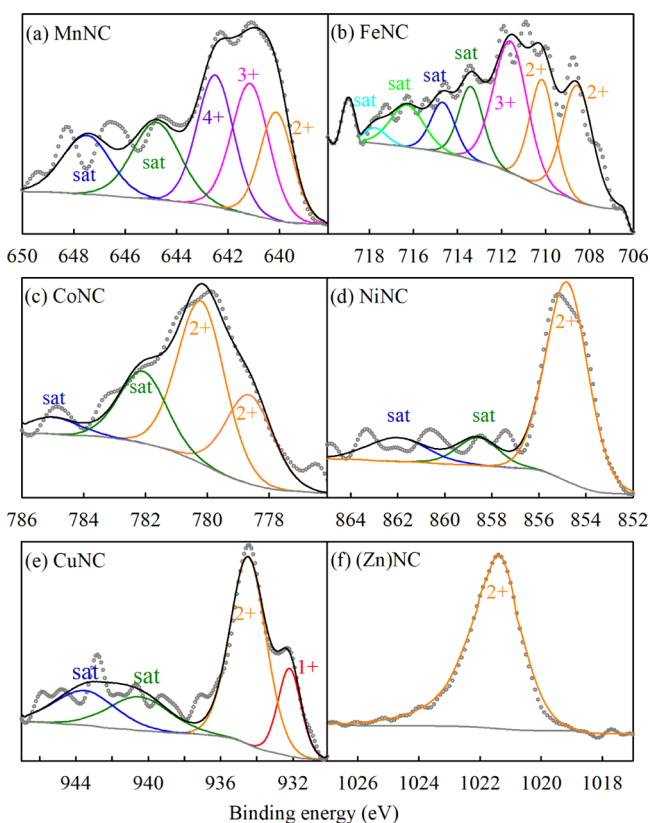


Figure 3. XPS characterization. Metal 2p spectra of (a) MnNC, (b) FeNC, (c) CoNC, (d) NiNC, (e) CuNC, and (f) (Zn)NC.

identify the coexistence of M^{2+} and M^{3+} species for FeNC, and the coexistence of M^+ and M^{2+} species for CuNC.^{57,58} Only the 2+ oxidation state is observed in CoNC, NiNC, and (Zn)NC, whereas for MnNC, the three different oxidation states 2+, 3+, and 4+ seem to be present.^{59–61} The existence of different oxidation states of the metal in a same catalyst reveals a structural and/or a topological heterogeneity of MN_x moieties. For example, higher oxidation states of the metal–cation might be triggered by oxygen (O_2 , OH) adsorbates, which is possible only for MN_x moieties located on the top surface, whereas those located in the bulk of the nitrogen-

doped carbon matrix are not accessible. Chemical heterogeneity might also lead to different oxidation states for a same structure. For example, whereas an average MN_4 structure was identified from our EXAFS analysis for all materials except FeNC (with additional oxygen adsorbates on top of the FeN_4 site itself), EXAFS cannot distinguish between N, O, and C atoms in the first coordination sphere, implying that, for example, MN_2O_2 moieties or any other combination with a total of four in-plane ligating atoms among C, N, and/or O are also possible structural candidates from an EXAFS viewpoint. Whereas the energetic stability of such moieties is usually lower than MN_4 ,^{62,63} their existence as minor species cannot be excluded. For MnNC in particular, the presence of high valence-state metal (4+) suggests that there might be some O atoms replacing N atoms in MnN_4 moieties. This will be re-discussed later.

The elemental content of the catalysts was quantified from XPS signals. All MNC catalysts have similar C, N, and O absolute contents, whereas the metal contents are in the range 0.16–0.27 at. %, except Zn in the range of 0.11 to 0.38 at. % (Table S2). The average nitrogen chemistry is similar for all five MNC catalysts with similar relative concentrations of different N species observed, as shown in Figure S6 and Table S3. Nitrogen–transition metal interactions are being expressed as a singular peak in the N 1s fine resolution spectra. Interactions of transition metal with 2, 3, or 4 co-planar N atoms are indistinguishable within the resolution of the peak composition analysis, as well as different transition metals studied here produce a de-facto identical shift, and the spectral component is commonly addressed here as $M-N_x$ (Figure S6). Nevertheless, a positive correlation was found between the N content and the total metal content of selected samples (Figure S7), with the linear fitting results for selected samples CuNC, ZnNC, NiNC and CoNC. MnNC was not included as we demonstrate that the first sphere coordination of Mn probably involves both O and N atoms (details will be discussed in Section 4.2), and FeNC was excluded from the linear fitting as it is, for an unknown reason, an outlier. Most interestingly, the fitted line in Figure S7 has a slope of 3.34 N atoms per metal atom, nicely supporting the fixation of close to four nitrogen atoms during pyrolysis per each single metal atom, and the major presence of MeN_4 sites for the (Zn)NC, CoNC, NiNC, and CuNC materials. The position of MnNC data point below the line also supports the mix of O and N in the first coordination sphere of Mn.

SEM (Figure S8) and N_2 physisorption isotherms (Figure S9) indicate a similar porous carbon structure in the six materials. The isotherm shape indicates a high microporosity (vertical rise at low P/P_0) and the existence of small mesopores that are responsible for the hysteresis. Similar porous structures had been observed on analogous ZIF-8-derived materials,^{22,23}

and micropores were shown to be important to host MN_x active sites.^{64,65} The Brunauer–Emmett–Teller surface areas of the catalysts are similar, in the range of 220–330 $m^2 g^{-1}$ (Table S4). Similar double layer capacitances according to CV further confirm that MNC and (Zn)NC materials possess a similar electrochemical surface area (Figure S10 and Table S4). As shown in Figure S1, the XRD patterns of the MNC catalysts revealed only two broad reflection peaks attributed to the (002) and (101) facets of nanometric graphitic structures.^{22,66} In the Raman spectra (Figure S11), all samples showed the same ratio of D to G band intensity ($I_D/I_G \approx 0.8$), suggesting the same degree of disorder of the carbon phase. In summary, the five MNC catalysts have similar structure and composition, with the only significant difference being the nature of the metal and its exact coordination and oxidation state in MN_x moieties.

3.2. Selectivity and Activity of MN_x Sites for eCO_2RR .

The catalytic activities of MNC and (Zn)NC toward eCO_2RR were first screened with LSV. The five MNC materials and also (Zn)NC exhibit higher current densities in CO_2 -saturated 0.1 M $KHCO_3$ than in N_2 -saturated 0.1 M K_2HPO_4/KH_2PO_4 buffer electrolyte (Figure S12). The onset potential is highest for FeNC, whereas the current density reached with NiNC surpassed that reached with FeNC below -0.8 V versus RHE (the reasons for the high onset of FeNC will be discussed later).¹⁴ CoNC shows even higher current density than NiNC at a low potential but, because of similarity in the polarization curves in CO_2 -saturated and CO_2 -free electrolytes (Figure S12c), this might mostly be attributed to HER. These trends agree with previous reports.^{14,15,20,21} The identification and quantification of the eCO_2RR products were then carried out under potentiostatic control. The FEs obtained from CA at -0.5 and -0.6 V versus RHE vary with the embedded metal center, as shown in Figure 4. Although CO was the major

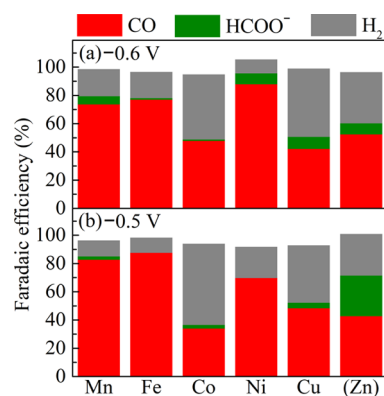


Figure 4. Product analysis. FE at (a) -0.6 V and (b) -0.5 V vs RHE obtained over the MNC catalysts ($M = Mn, Fe, Co, Ni,$ and Cu), plotted against the embedded metal center sorted by the atomic number. The data were obtained by CA for 90 min, performed in 0.1 M $KHCO_3$ aqueous electrolyte saturated with CO_2 (pH 6.7) at room temperature.

eCO_2RR product over all MNC, the highest FEs were observed over the Fe-, Ni- and Mn-NC materials. High FEs have been reported previously for other FeNC^{10,17,20,67} and NiNC^{13,16,18,19,38} materials synthesized via different approaches but sharing a key common structural feature, namely, the atomically dispersed MN_x moieties. Also, in agreement with other recently published results, the major

product over CoNC is H_2 .^{14,15,20,21} On the contrary, high selectivity (more than 90%) toward CO_2 reduction to CO in a wide potential range (-0.57 to -0.88 V vs RHE) over atomically dispersed CoN_x was reported as well,^{68,69} but with slightly different coordination environment. As the present series of MNC and (Zn)NC catalysts has, except for the nature of the metal element in MN_x moieties, negligible difference in morphology and structure, the different activity and selectivity toward eCO_2RR to CO can be mainly ascribed to the nature of the metal in MN_x sites. Last, (Zn)NC shows a selectivity for CO being in-between the low value of CoNC and the high values of MnNC, FeNC, and NiNC.

Although Figure 4 indicates the relative fraction of all products formed during CA on each of the catalysts, it does not convey any information on the rate at which these products formed. Therefore, the partial current densities for each of the products ($CO, HCOO^-,$ and H_2) were calculated from the CA data, and are reported in Figure 5. They were

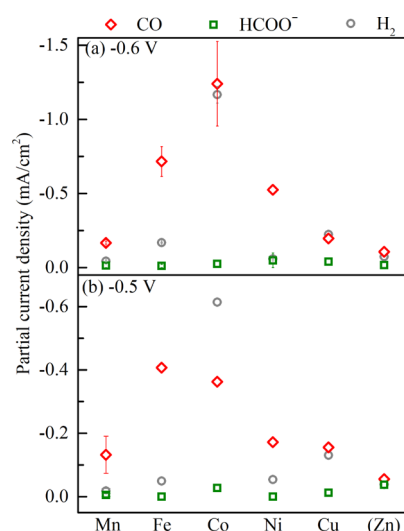


Figure 5. Volcano trend in eCO_2RR activity. Partial current densities at (a) -0.6 V and (b) -0.5 V vs RHE over the MNC catalysts for $CO, HCOO^-,$ and H_2 products. The data were obtained by CA for 90 min, in 0.1 M $KHCO_3$ saturated with CO_2 (pH 6.7) at room temperature.

calculated from the knowledge of (i) the average current density on each catalyst during the CA experiment and (ii) the product quantification averaged during the CA (see Experimental Methods). Looking at the results obtained at -0.6 V versus RHE (Figure 5a), it should first be noted that, whereas (Zn)NC shows non-zero activity toward CO_2 reduction, it is negligible compared to the activity observed for FeNC, CoNC, and NiNC. The low activity of (Zn)NC is attributed to ZnN_4 moieties^{8,70} and/or nitrogen groups not bonded to any metal.^{71,72} Given that MNC catalysts and (Zn)NC share a similar carbon matrix with similar amounts of ZnN_4 moieties and nitrogen functionalities, we assign the higher partial current densities for CO formation (J_{CO}) of MNC samples to the presence of MN_x moieties (Fe-, Co-, and NiN_x moieties in particular). A catalytic synergy between MN_x and ZnN_4 moieties is also unlikely when the main considered product of CO_2 reduction is CO (only two electrons transferred, with $COOH^*$ as the only possible intermediate species). There are generally three steps for the eCO_2RR to CO: (i) $CO_2 + H^+ + e^- \rightarrow COOH^*$ (this first electron and proton transfer can be

further decoupled into two steps: (i-a) $\text{CO}_2 + \text{e}^- \rightarrow \text{CO}_2^{*-}$, and (i-b) $\text{CO}_2^{*-} + \text{H}^+ \rightarrow \text{COOH}^*$, as discussed in the following DFT simulations), (ii) $\text{COOH}^* + \text{H}^+ + \text{e}^- \rightarrow \text{CO}^* + \text{H}_2\text{O}$ and (iii) CO^* desorption. If a synergistic effect between MN_x and ZnN_4 moieties occurs, there are two possibilities: (a) MN_x catalyzes step (i) and ZnN_4 catalyzes step (ii); or (b) the opposite. Assuming the synergy case (a), the FE for formate on FeNC, CoNC and NiNC should be significantly higher than that on (Zn)NC, which is not the case (Figure 4). Assuming the synergy case (b), (Zn)NC should have a J_{HCOO^-} value comparable to J_{CO} observed on the active catalysts NiNC, FeNC, and CoNC. However, this is also in contrast with experimental results, where J_{HCOO^-} on (Zn)NC is negligible compared to J_{CO} on NiNC, FeNC, and CoNC (Figure 5). Thus, we can rule out any significant catalysis synergy between MN_x and ZnN_4 moieties.

Interestingly, with increasing atomic number from Mn to Co, J_{CO} monotonically increases, whereas with further increasing atomic number of the metal, the J_{CO} value decreases (Figure 5a). A volcano-shaped trend is thus identified in the electrocatalytic activity for the reduction of CO_2 to CO. A similar volcano trend is also apparent at -0.5 V versus RHE, but with FeNC exhibiting a slightly higher J_{CO} value than CoNC at this potential (Figure 5b). The same volcano trends are observed if J_{CO} is normalized by the electrochemical double layer capacitance (Figure S13b) or by the metal content obtained from XPS (Figure S13c). These observations indicate that MN_x moieties embedded in the nitrogen-doped carbon matrix exhibit not only different selectivity but also distinct activities toward eCO_2RR . Herein, we for the first time reveal a volcano-shaped trend in the electrocatalytic activity for the CO_2 to CO reduction over a series of pyrolyzed MNC catalysts, with CoNC and FeNC located at the volcano peak at -0.6 and -0.5 V versus RHE, respectively. The underlying reasons for this volcano-trend are discussed in the next section.

The DFT simulations were performed on the most likely oxidation state and environment for each of the metals. Although it was characterized via ex situ XPS, the oxidation state under operating conditions might be very different.^{24,67} We therefore resorted to operando XANES spectroscopy to track possible changes in the oxidation state of MN_x sites during eCO_2RR . The overlapping XANES spectra at OCP before and after CA at 0.0, -0.5 , -0.6 and -1.0 V versus RHE demonstrate that no irreversible structural change occurred for the MN_x sites during eCO_2RR (Figure 6a), in agreement with operando XAS results on other MNC catalysts previously reported.^{24,67} The position of the absorption edge at the metal K-edge XANES spectra is generally recognized to correlate, for a given coordination environment of the metal, to the metal oxidation state. The absorption edge position was therefore determined as the maximum of the first derivative of the XANES spectra, and is shown as a function of the electrochemical potential in Figure 6b. The figure indicates that a reduction occurred for Fe, Ni, and Cu sites when decreasing the potential from OCP to -0.5 V versus RHE, whereas the oxidation state of Mn and Co sites remained the same. Combined with the ex situ XPS oxidation state identification, we can infer that the oxidation state of Fe was modified from 2+/3+ to only 2+, that of Ni reduced from 2+ to 1+, and that of Cu reduced from 2+/1+ to 0.^{14,73} The oxidation state of Mn remained a mixture of 2+/3+/4+, and that of Co remained as 2+, even at -1.0 V versus RHE. It can further be observed that Fe was reduced from a mix of 2+/3+

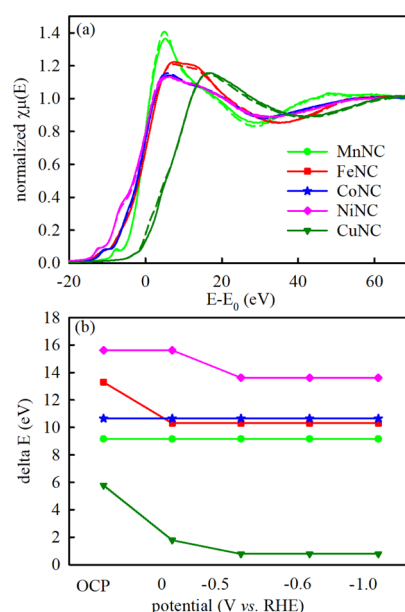


Figure 6. (a) Metal K-edge XANES spectra of MNC catalysts at OCP before and after the CA measurements at different potentials (solid curve: before; dashed curve: after), and (b) change in the absorption edge of metal K-edge XANES spectra of MNC catalysts with applied potential. The electrolyte was CO_2 -saturated 0.1 M KHCO_3 , and the OCP was around 0.7 V vs RHE. In (a), the x-axis is the difference between the X-ray energy and the absorption edge of MNC (E_0). In (b), the y-axis (ΔE) is ($E_0 - E_{0,\text{metal}}$).

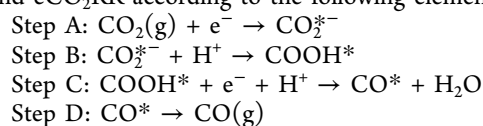
to only 2+ already at 0 V versus RHE, in line with the redox potential identified for FeNC at ca. 0.75 V versus RHE in acidic electrolyte.^{22,74} This may explain the high onset potential for eCO_2RR over FeNC, whereas NiNC is possibly inactive for eCO_2RR as long as it is in 2+ oxidation state (discussed later in combination with DFT). The changes in oxidation states of the three most active MNC catalysts (namely Fe, Co, and Ni) with applied potential agree well with the calculated Pourbaix speciation diagrams, which shows that in a pH = 7 electrolyte, the oxidation state of Fe and Co in MN_4 corresponds to Co^{2+} at any potential < 0 V versus RHE, whereas there is a reduction from Ni^{2+} to Ni^{1+} below 0 V versus RHE at pH = 7 (Figure S14), in line with the Ni-reduction experimentally observed between 0 and -0.5 V versus RHE experimentally (Figure 6b). It should be noted that XAS is a bulk technique and therefore the signal and values reported in Figure 6 are an average of all metal atoms of the same nature in the sample, regardless of whether they are on the surface (sensitive to the electrochemical potential) or in the bulk (possibly insensitive to the electrochemical potential).

4. DISCUSSION

4.1. Explanation for the Slightly Different Volcano Trends at -0.5 and -0.6 V Versus RHE. Figure 5 reveals that the most active catalyst for eCO_2RR to CO depends on the electrochemical potential. In the general case, such a potential-dependent volcano trend can be expected, as the electrochemical kinetics of even a simple one-electron reaction is governed by at least two parameters, namely, the exchange current density (i_0) and the Tafel slope. Only if the Tafel slope for eCO_2RR to CO is the same on all MNC catalysts can one expect a potential-independent activity trend. This is clearly shown in Figure S15, constructed from Tafel laws and

assuming different i_0 values and either a common Tafel slope (Figure S15a) or slightly different Tafel slopes (Figure S15b). The plot of the kinetic current density versus potential show the same trends at -0.5 and -0.6 V versus RHE when the Tafel slope is assumed to be the same for all three catalysts (Figure S15c), whereas the trends differ when different Tafel slopes are assumed (Figure S15d). Thus, the simplest explanation to account for the slightly different volcano trends in Figure 5a,b is a variation of the eCO₂RR Tafel slope from one catalyst to another. This may, in turn, be related to different rate-determining steps of eCO₂RR on those different catalysts. From the theory of electrokinetics of multielectron reactions, higher Tafel slopes are generally expected when the rate-determining step (RDS) is the first electron transfer than when it is the second electron transfer or any reaction step after the second electron transfer.⁷⁵

4.2. Underlying Reason for the Volcano Trends. The observation of volcano trends in the electrochemical activity for various reactions among a series of metal-based catalysts with similar site structures is generally explained by Sabatier's principle, with the binding energy of the metal sites being tuned by the metal's atomic number, and leading to too weak, optimum, and too strong binding of the key intermediate-adsorbed species when moving in a given direction in the series of transition metal.^{76,77} We then performed DFT calculations with MN₄C₁₀ model (M = Mn, Fe, Co, Ni, and Cu, with axial oxygen adsorbates for some of the metals) with the CHE model at $U = -0.6, -0.5,$ and 0.0 V versus RHE, to investigate the binding energy of the key reaction intermediates for HER and eCO₂RR according to the following elementary steps



The reaction energy profiles for each elementary step of eCO₂RR (Figure 7 ($U = -0.6$ and -0.5 V vs RHE), Figure S16 ($U = 0.0$ V vs RHE) and Tables S5–S7) show that the particular transition metal present in the N₄ lattice has a tremendous effect on reactivity. As eCO₂RR does not occur at $U = 0.0$ V versus RHE, we focus in our discussion on the free energy diagrams at $U = -0.6$ and -0.5 V versus RHE (Figure 7), potentials at which we experimentally measured the eCO₂RR activity and selectivity of MNC catalysts. Overall, the calculated Gibbs free energy diagrams demonstrate that MnN₄ and FeN₄ bind CO too strongly and their CO production rate is determined by the CO* desorption step. In contrast, NiN₄ and CuN₄ have weak CO binding energy, and the CO₂ activation and first electron transfer then becomes the RDS (Table S8). In this series of model sites, CoN₄ shows the optimum balance between the energy barriers for CO₂ activation and CO desorption (steps A and D in Table S8, respectively).

We also investigated how axial adsorbates (H₂O, OH, and O) affect the reaction energies on MnN₄, FeN₄, and CoN₄ (no oxygen adsorbates could be stabilized on CuN₄ and NiN₄). Particularly, the H₂O molecule axially adsorbed on FeN₄ lowers the reaction barrier for the first electron transfer to form CO₂²⁻ (Figures 7b and S14) and thus promotes the eCO₂RR to CO over FeNC. In this case, FeN₄ sites are approachable from both axial directions (one side for adsorbing H₂O, and the other side for activating CO₂ gas molecule). Moreover, for the case of NiNC, NiN₄C₁₀ with oxidation states of 1+ and 2+ are both used in the DFT

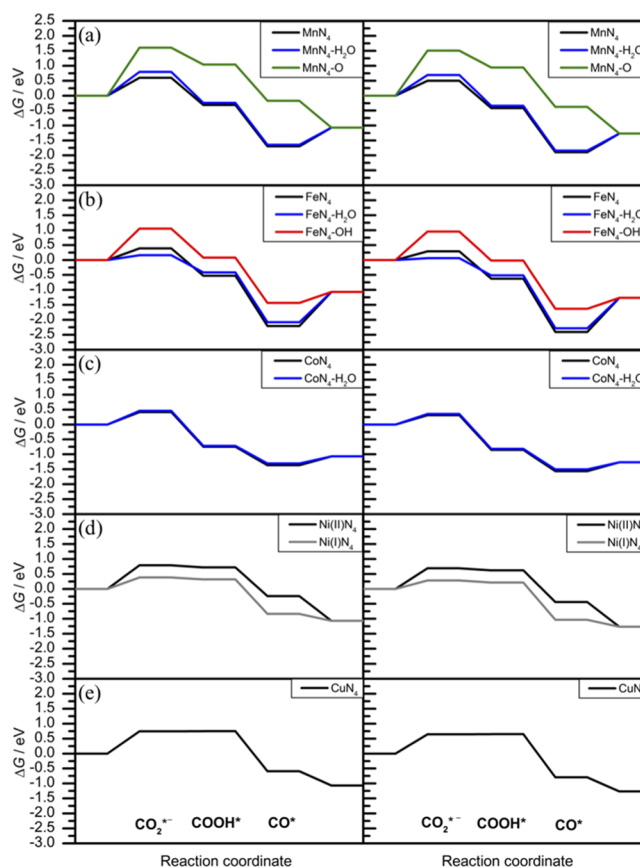


Figure 7. Gibbs free energy profiles for eCO₂RR over MN₄ model sites ((a–e) M = Mn, Fe, Co, Ni, and Cu) at $U = -0.5$ V (left) and -0.6 V (right) vs RHE (pH = 7) according to the different metal speciation (oxidation state and ligand coordination).

simulations, as a reduction of Ni²⁺ to Ni¹⁺ was observed from operando XAS (Figure 6). In contrast to the high energy barrier for the CO₂ activation on Ni²⁺N₄C₁₀ (the first step for eCO₂RR), Ni¹⁺N₄C₁₀ binds CO₂ more strongly (Figure 7d). This explains that the onset potential of eCO₂RR over NiNC is highly correlated to the Ni^{2+/1+}N₄ redox potential (Figures 6b and S11d). The CO₂ activation energies are also highly correlated to the geometries of the CO₂ coordination over MN₄ sites, as depicted in Figure S17 showing how CO₂ is activated in the Fe, Co, and Ni sites. Whereas both a M–C and a M–O bonds can simultaneously form with the FeN₄ active site, only a M–C bond appears for the CoN₄ and NiN₄ sites. In addition, the O–C–O angle departs from the 180° value in the gas phase to only 145° when adsorbed on FeN₄. This explains the lower activation energy of CO₂ over FeNC versus other MNC catalysts and the higher onset potential for FeNC.

The activity trends for CO₂ reduction to CO can be estimated from DFT calculations on the basis of the exergonic value of the reaction energy at the RDS. Table S8 reports the reaction energy calculated for each elementary step for MN₄(–H₂O) moieties according to the Gibbs free energy profiles for eCO₂RR over MNC catalysts (M = Mn, Fe, Co, Ni, and Cu) at $U = -0.6$ V versus RHE. For each MN₄ site, the structure (with/without H₂O adsorbate) with lowest reaction energy at the RDS is considered in Table S8. To compare DFT results to the experimental eCO₂RR activity trend, we assumed an Arrhenius type law of the form $A \exp(-E_{\text{RDS}}/RT)$, where E_{RDS} is the free energy change at the RDS and A is a pre-

exponential factor, assumed the same for all MNC catalysts investigated because of similar metal content and similar carbon porosity, chemistry, and morphology. Figure 8 shows

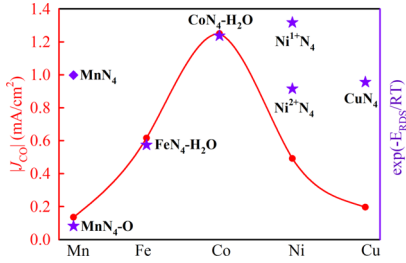


Figure 8. Comparison of experimental CO partial current density at -0.6 V vs RHE for pyrolyzed MNC materials and DFT calculated trends ($U = -0.6$ V vs RHE). E_{RDS} is the calculated free reaction energy at the specific RDS of $e\text{CO}_2\text{RR}$ to CO for each active site (see Table S8).

that the trend of reaction rate predicted from DFT according to this approach matches well the experimentally observed volcano trend in the present work, except for MnN_4 and CuN_4 , which will be discussed later. Among all the $\text{MN}_4(-\text{H}_2\text{O})$ active sites, Ni^{1+}N_4 is predicted to show the highest activity toward $e\text{CO}_2\text{RR}$ to CO, with lowest maximum for the free reaction energy at any of the elementary steps. However, the experimental oxidation states of NiN_4 sites are most likely in a mix of $1+/2+$ at -0.6 V versus RHE (Figures 6 and S12). Thus, the experimental activity of NiNC should fall between those predicted for Ni^{1+}N_4 and Ni^{2+}N_4 . Experimentally, the $e\text{CO}_2\text{RR}$ activity of NiNC is even lower than that estimated

from DFT for Ni^{2+}N_4 however. We assign this to a lower onset potential for NiNC than for CoNC, but once the reaction has started, recent studies have shown that NiNC catalysts with single metal atom sites are the most active and selective MNC catalysts reported to date.^{13,16,18,19,38} The calculated activity trends for MN_4 sites are as following $\text{FeN}_4-\text{H}_2\text{O} < \text{MnN}_4 < \text{CoN}_4-\text{H}_2\text{O} < \text{Ni}^{1+}\text{N}_4 > \text{Ni}^{2+}\text{N}_4 \approx \text{CuN}_4$, with metals on the left-hand side of Co or Ni binding CO too strongly, and metals on the right-hand side binding CO_2 too weakly.

One discrepancy between the present experimental results and theoretical results is MnNC, for which our experimental results show much lower CO partial current density than FeNC, whereas the DFT calculations predicted that MnN_4 and FeN_4 sites are both limited by the CO^* desorption step, but with lower desorption barrier for MnN_4 . This results in a predicted $e\text{CO}_2\text{RR}$ activity higher for MnN_4 than FeN_4 moieties (Figure 8).

Given that a higher oxidation state of Mn (a mixture of $4+$, $3+$, and $2+$) was observed by ex situ XPS and operando XANES than can be assumed with a MN_4 model site, and given that MnN_x has a higher predicted affinity to oxygen,⁵³ we re-evaluated the possible active site structure of MnNC. We assumed MnN_2O_2 as an alternative model site (Figure S18a). Both MnN_4 and MnN_2O_2 structures converged and optimized under the same conditions, confirming similar energy stabilities of these two structures. Moreover, the experimental FT-EXAFS spectrum of MnNC could be properly fitted with the MnN_2O_2 model site (Figure S18b), and its DFT calculated EXAFS spectrum (Figure S18c) exhibits the same characteristic peak at ~ 1.5 Å assigned to both N and O back-scattering from the first coordination sphere. According to our DFT

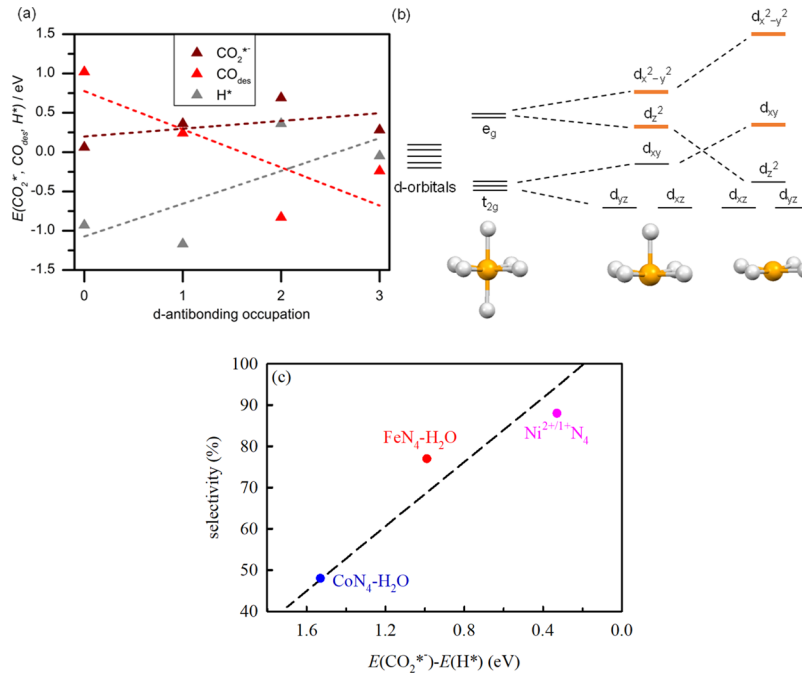


Figure 9. Relationship between the adsorption/desorption energies and the local electronic configurations on the Fe, Co, and Ni ($1+$ and $2+$). (a) CO_2^{*-} (wine), H^* (gray) adsorption energies and CO (red) desorption (at $\text{pH} = 7$, $U = -0.6$ V) as a function of the d-antibonding occupation in the active site. In (b), the symmetry descent from the octahedral configuration to either square pyramid or square planar is shown (orange indicates the antibonding states). For the most common Fe species under potential Fe and Co are in $\text{MN}_4-\text{H}_2\text{O}$ (square pyramid with 0 and 1 antibonding electrons). Instead, Ni is in the square planar configuration with already two electrons in the antibonding state. At high negative potential the highest antibonding $d_{x^2-y^2}$ would be occupied, which could trigger the distortion of the planar pocket (Ni^{1+} state). (c) The experimental selectivity at -0.6 V vs RHE over FeNC, CoNC, and NiNC vs the DFT-simulated $E(\text{CO}_2^{*-}) - E(\text{H}^*)$.

calculations, this MnN_2O_2 model can however not coordinate CO_2 and is therefore predicted to be inactive toward eCO_2RR . Even with a single oxygen adsorbate, the MnN_4 site becomes poorly active toward eCO_2RR , as indicated by the very high energy barrier for CO_2 adsorption calculated by DFT for the $\text{MnN}_4\text{-O}$ model (Figure 7a). Of all the Mn models investigated, only Mn^{2+} without oxygen ligands can effectively coordinate CO_2 . However, as identified by ex situ XPS and operando XANES (Figures 3 and 6), this species is uncommon at the investigated potentials, explaining why no activity is experimentally found for MnNC. Last, for CuNC, our operando XANES data show that Cu switches from 2+ to 0 oxidation state early on (Figure 6), explaining the mismatch between DFT predictions and the experimental CuNC activity. In summary, with the $\text{MnN}_4\text{-O}$ model site for MnNC and $\text{MN}_4\text{C}_{10}(\text{-H}_2\text{O})$ model sites for other MNC catalysts ($M = \text{Fe, Co, Ni}$), the experimental volcano trend in the eCO_2RR to CO activity of MNC catalysts can be nicely explained by our DFT-calculated Gibbs free energy for the RDS (Figure 8).

The volcano-shaped trend in eCO_2RR activity to CO over various MNC catalysts could not be identified in other reports, where CoNC exhibited lower J_{CO} values relative to other MN_x moieties (Ni and Fe in particular) in a broad potential range.^{14,15,21} The reason for this seems to be that previous reports either lacked evidence for the exclusive atomically dispersed nature of transition metals (the XRD for some of the MNC catalysts exhibited sharp peaks arising from metallic nanoparticles, which might alter the carbon structure),^{14,15} or studied the activity of MNC catalysts varying not only in the nature of the transition metal but also in the carbon matrix structure (as shown in XRD and/or N_2 adsorption/desorption isotherms).²¹

4.3. Selectivity toward CO over MN_4 . As another critical factor for a good eCO_2RR catalyst, selectivity is highly correlated to the H^* and CO_2^{*-} binding energies over MN_x active sites. Thus, we investigated the Gibbs free energy profiles of HER over MN_4C_{10} model sites ($M = \text{Mn, Fe, Co, Ni, and Cu}$) at -0.5 and -0.6 V versus RHE (Figure S19).

These binding energies can be rationalized from simple coordination chemistry rules. The adsorption behavior for the metals in the first transition series depends on the occupation of antibonding d-orbitals coming from the crystal field splitting for the resting square pyramidal structure. Therefore, we use the number of d-antibonding electrons (0 for $\text{FeN}_4\text{-H}_2\text{O}$, 1 for $\text{CoN}_4\text{-H}_2\text{O}$, 2 for Ni^{1+}N_4 , and 3 for Ni^{2+}N_4) to explain the selectivity toward eCO_2RR to CO over MN_4 sites (Figure 9). The population of the antibonding states results from counting the number of electrons in the d-orbitals of the ground-state configuration according to the crystal field splitting theory. Figure 9a indicates that there is a linear scaling relationship between the CO_2^{*-} and CO^* binding energies (Figure S20), which determines the CO activity. Thus, the CO binding energy can serve as a key descriptor for eCO_2RR to CO activity. The volcano trend with CO binding energy as a descriptor (J_{CO} measured experimentally vs CO binding energy calculated from DFT simulations) is shown in Figure S21, with Fe located at the strong binding branch, whereas Ni and Cu are on the weak binding branch. $\text{CoN}_4\text{-H}_2\text{O}$ sites possess the optimum binding energies with CO^* , which are neither too strong nor too weak. On the other hand, good selectivity toward CO requires high CO_2^{*-} binding energy and low H^* binding energy (the more negative value in Figure 9a, the higher the binding energy). Thus, we utilized the difference of

CO_2^{*-} and H^* binding energies ($E(\text{CO}_2^{*-}) - E(\text{H}^*)$) as the descriptor for selectivity (Figure 9c). In that figure, we show only the experimental data for FeNC, NiNC, and CoNC and did not include the other MNC materials, whose eCO_2RR activity and selectivity can originate in whole or in part from metal-free nitrogen functional groups.⁷⁸ The $\text{CoN}_4\text{-H}_2\text{O}$ site has an optimum binding energy with CO_2^{*-} , but, unfortunately, the binding energy of H^* is much higher than that of CO_2^{*-} , which leads to a low selectivity toward CO, in line with the experimental result on CoNC (48%, Figure 9c). The high selectivity of eCO_2RR to CO over NiN_4 benefits from the lower H^* binding energies compared to other MN_4 sites (Figure 9c). For $\text{FeN}_4\text{-H}_2\text{O}$, even though the high binding energy to H^* suggests a high HER activity (Figure 9a), the reduction of CO_2 to CO^* also occurs with zero energy barrier, and the binding energy of CO^* on $\text{FeN}_4\text{-H}_2\text{O}$ is much stronger than that of H^* on $\text{FeN}_4\text{-H}_2\text{O}$. Thus, the majority of FeN_4 sites are occupied by CO^* in CO_2 -saturated electrolyte. This site-blocking effect probably suppresses the binding of such active sites with HER-related species, resulting in high experimental selectivity toward CO over FeNC. As can be seen in Figure 9c, the selectivity of eCO_2RR toward CO over MN_x moieties can be explained with the DFT-calculated CO_2^{*-} and H^* binding energies, that in turn are highly correlated to the number of d-antibonding electrons. The latter descriptor can thus be used to screen for more promising eCO_2RR candidate MNC materials.

5. CONCLUSIONS

The careful integration of experimental and theoretical methods allowed us to establish clear correlations between physicochemical and catalytic properties for the eCO_2RR of atomically dispersed MN_4 centres ($M = \text{Mn, Fe, Co, Ni, and Cu}$). The ex situ characterization demonstrates the incorporation of the metal exclusively in MN_4 centers over otherwise similar nitrogen-doped carbon matrices. Ex situ XPS and in situ XANES were applied to identify and monitor changes of the metal oxidation state at rest and under operating conditions, respectively. Mn and Co did not change oxidation state down to -1.0 V versus RHE, whereas Fe and Ni were partially reduced and Cu was largely reduced to a metallic state. Over these highly controlled systems, catalytic tests revealed a volcano-like dependency between eCO_2RR activity and the atomic number of the transition metal, with Fe and Co as the most active centers. In contrast, no clear trend was observable for the FE toward CO, for which Fe, Mn, and Ni-based materials showed the highest values (>80%). Computational models led to the identification of active centers and finally to descriptors rationalizing the distinct activity and selectivity patterns observed. To this end, different configurations were studied according to the speciation of the metal atom, its charge, spin, and coordination sphere. Among the best performing materials, $\text{Fe}^{2+}\text{N}_4\text{-H}_2\text{O}$ and $\text{Co}^{2+}\text{N}_4\text{-H}_2\text{O}$ centers were found as the most likely active catalytic centers at considered potentials (-0.5 and -0.6 V vs RHE), whereas Ni^{1+}N_4 was predicted as the most active Ni-based one. The Gibbs free energy change at the RDS accounted for the experimentally determined activity volcano, with Co-, Fe-, and Ni-based systems showing the best compromise between CO^* and CO_2^{*-} binding energies. Regarding selectivity, the difference between the binding energies for CO_2^{*-} and H^* , directly related to the number of d-antibonding electrons, described successfully the high selectivity observed on Fe- and

Ni catalysts and the more favored HER observed over the Co-based one. All in all, these results describe the influence of the particular metal species existing at relevant potentials on the catalytic activity and selectivity, laying down the path for a rational optimization of single-atom catalysts for eCO₂RR.

■ ASSOCIATED CONTENT

5 Supporting Information

The Supporting Information is available free of charge on the

Physical (XRD, (S)TEM, EDX, XAS, XPS, SEM, N₂ physisorption, and Raman) and electrochemical (CV, LSV) characterizations of MNC catalysts, the calculated electrochemical potential versus logarithm of the reaction rate with simplified Tafel laws, and the DFT calculated Gibbs free energy diagrams of eCO₂RR to CO and HER (PDF)

■ AUTHOR INFORMATION

Corresponding Author

*E-mail: frederic.jaouen@umontpellier.fr.

ORCID

Jingkun Li: 0000-0002-8679-9612

Tatsuya Shinagawa: 0000-0002-5240-7342

Frank Krumeich: 0000-0001-5625-1536

Kateryna Artyushkova: 0000-0002-2611-0422

Plamen Atanassov: 0000-0003-2996-472X

Andrea Zitolo: 0000-0002-2187-6699

Rodrigo García-Muelas: 0000-0002-2219-5027

Núria López: 0000-0001-9150-5941

Javier Pérez-Ramírez: 0000-0002-5805-7355

Frédéric Jaouen: 0000-0001-9836-3261

Present Address

[∇]School of Engineering, Department of Chemical System Engineering, The University of Tokyo, 7-3-1 Hongo, Bunkyo-ku, 113-8656, Tokyo, Japan.

Author Contributions

J.L. and F.J. designed, synthesized, and physically characterized the materials. T.S., A.J.M.F., and J.P.-R. performed the eCO₂RR electrochemical measurements and product analysis. P.P., Y.Z., R.G.-M., and N.L. performed the DFT simulations. F.K. conducted the (S)TEM and EDX characterizations. A.Z. conducted the XAS analysis and computation. K.A. and P.A. conducted the XPS measurement and analysis. J.L. and F.J. wrote and edited the paper with input from all authors. All authors read and approved the final version of the paper.

Funding

The research leading to these results has received funding from the A-LEAF Project, which is funded by the European Union's H2020 Programme under grant agreement no. 732840. We thank the BSC-RES for providing generous computational resources. Additional financial support was generously provided by the MCIU/AEI/FEDER/UE RTI2018-101394-B-I00 and AGAUR 2017-SGR-90 projects. P.P. thanks ITN-ELCOREL (funded by the European Union's H2020 Programme under grant agreement No. 722614) for a predoctoral grant.

Notes

The authors declare no competing financial interest.

■ ACKNOWLEDGMENTS

We acknowledge Synchrotron SOLEIL (Gif-sur Yvette, France) for provision of synchrotron radiation facilities at beamline SAMBA (proposal number 20180635) and the Scientific Center for Optical and Electron Microscopy (ScopeM) of ETH Zurich for access to its facilities.

■ REFERENCES

- (1) Zheng, T.; Jiang, K.; Wang, H. Recent Advances in Electrochemical CO₂ to CO Conversion on Heterogeneous Catalysts. *Adv. Mater.* **2018**, *30*, 1802066.
- (2) Larrazábal, G. O.; Martín, A. J.; Pérez-Ramírez, J. Building Blocks for High Performance in Electrocatalytic CO₂ Reduction: Materials, Optimization Strategies, and Device Engineering. *J. Phys. Chem. Lett.* **2017**, *8*, 3933–3944.
- (3) Wang, Y.; Liu, J.; Wang, Y.; Al-Enizi, A. M.; Zheng, G. Tuning of CO₂ Reduction Selectivity on Metal Electrocatalysts. *Small* **2017**, *13*, 1701809.
- (4) Martín, A. J.; Larrazábal, G. O.; Pérez-Ramírez, J. Towards Sustainable Fuels and Chemicals Through the Electrochemical Reduction of CO₂: Lessons from Water Electrolysis. *Green Chem.* **2015**, *17*, S114–S130.
- (5) Zhang, W.; Hu, Y.; Ma, L.; Zhu, G.; Wang, Y.; Xue, X.; Chen, R.; Yang, S.; Jin, Z. Progress and Perspective of Electrocatalytic CO₂ Reduction for Renewable Carbonaceous Fuels and Chemicals. *Adv. Sci.* **2018**, *5*, 1700275.
- (6) Lin, S.; Diercks, C. S.; Zhang, Y.-B.; Kormienko, N.; Nichols, E. M.; Zhao, Y.; Paris, A. R.; Kim, D.; Yang, P.; Yaghi, O. M.; Chang, C. J. Covalent Organic Frameworks Comprising Cobalt Porphyrins for Catalytic CO₂ Reduction in Water. *Science* **2015**, *349*, 1208–1213.
- (7) Zhang, Z.; Xiao, J.; Chen, X. J.; Yu, S.; Yu, L.; Si, R.; Wang, Y.; Wang, S.; Meng, X.; Wang, Y.; Tian, Z. Q.; Deng, D. Reaction Mechanisms of Well-Defined Metal-N₄ Sites in Electrocatalytic CO₂ Reduction. *Angew. Chem., Int. Ed.* **2018**, *57*, 16339–16342.
- (8) Wu, Y.; Jiang, J.; Weng, Z.; Wang, M.; Broere, D. L.; Zhong, Y.; Brudvig, G. W.; Feng, Z.; Wang, H. Electroreduction of CO₂ Catalyzed by a Heterogenized Zn–Porphyrin Complex with a Redox-Innocent Metal Center. *ACS Cent. Sci.* **2017**, *3*, 847–852.
- (9) Costentin, C.; Drouet, S.; Robert, M.; Savéant, J.-M. A Local Proton Source Enhances CO₂ Electroreduction to CO by a Molecular Fe Catalyst. *Science* **2012**, *338*, 90–94.
- (10) Huan, T. N.; Ranjbar, N.; Rousse, G.; Sougrati, M.; Zitolo, A.; Mougél, V.; Jaouen, F.; Fontecave, M. Electrochemical Reduction of CO₂ Catalyzed by Fe-NC Materials: A Structure–Selectivity Study. *ACS Catal.* **2017**, *7*, 1520–1525.
- (11) Han, N.; Wang, Y.; Ma, L.; Wen, J.; Li, J.; Zheng, H.; Nie, K.; Wang, X.; Zhao, F.; Li, Y.; Fan, J.; Zhong, J.; Wu, T.; Miller, D. J.; Lu, J.; Lee, S.-T.; Li, Y. Supported Cobalt Polyphthalocyanine for High-Performance Electrocatalytic CO₂ Reduction. *Chem* **2017**, *3*, 652–664.
- (12) Manbeck, G. F.; Fujita, E. A Review of Iron and Cobalt Porphyrins, Phthalocyanines and Related Complexes for Electrochemical and Photochemical Reduction of Carbon Dioxide. *J. Porphyrins Phthalocyanines* **2015**, *19*, 45–64.
- (13) Yang, H. B.; Hung, S.-F.; Liu, S.; Yuan, K.; Miao, S.; Zhang, L.; Huang, X.; Wang, H.-Y.; Cai, W.; Chen, R.; Gao, J.; Yang, X.; Chen, W.; Huang, Y.; Chen, H. M.; Li, C. M.; Zhang, T.; Liu, B. Atomically Dispersed Ni(I) as the Active Site for Electrochemical CO₂ Reduction. *Nat. Energy* **2018**, *3*, 140–147.
- (14) Ju, W.; Bagger, A.; Hao, G.-P.; Varela, A. S.; Sinev, I.; Bon, V.; Cuenya, B. R.; Kaskel, S.; Rossmeisl, J.; Strasser, P. Understanding Activity and Selectivity of Metal-Nitrogen-Doped Carbon Catalysts for Electrochemical Reduction of CO₂. *Nat. Commun.* **2017**, *8*, 944.
- (15) Pan, F.; Deng, W.; Justiniano, C.; Li, Y. Identification of Champion Transition Metals Centers in Metal and Nitrogen-Codoped Carbon Catalysts for CO₂ Reduction. *Appl. Catal., B* **2018**, *226*, 463–472.

- (16) Li, X.; Bi, W.; Chen, M.; Sun, Y.; Ju, H.; Yan, W.; Zhu, J.; Wu, X.; Chu, W.; Wu, C.; Xie, Y. Exclusive Ni–N₄ Sites Realize Near-Unity CO Selectivity for Electrochemical CO₂ Reduction. *J. Am. Chem. Soc.* **2017**, *139*, 14889–14892.
- (17) Varela, A. S.; Kroschel, M.; Leonard, N. D.; Ju, W.; Steinberg, J.; Bagger, A.; Rossmeisl, J.; Strasser, P. pH Effects on the Selectivity of the Electrocatalytic CO₂ Reduction on Graphene-Embedded Fe–N–C Motifs: Bridging Concepts Between Molecular Homogeneous and Solid-State Heterogeneous Catalysis. *ACS Energy Lett.* **2018**, *3*, 812–817.
- (18) Jiang, K.; Siahrostami, S.; Zheng, T.; Hu, Y.; Hwang, S.; Stavitski, E.; Peng, Y.; Dynes, J.; Gangisetty, M.; Su, D.; Attenkofer, K.; Wang, H. Isolated Ni Single Atoms in Graphene Nanosheets for High-Performance CO₂ Reduction. *Energy Environ. Sci.* **2018**, *11*, 893–903.
- (19) Zhao, C.; Dai, X.; Yao, T.; Chen, W.; Wang, X.; Wang, J.; Yang, J.; Wei, S.; Wu, Y.; Li, Y. Ionic Exchange of Metal–Organic Frameworks to Access Single Nickel Sites for Efficient Electroreduction of CO₂. *J. Am. Chem. Soc.* **2017**, *139*, 8078–8081.
- (20) Pan, F.; Zhang, H.; Liu, K.; Cullen, D.; More, K.; Wang, M.; Feng, Z.; Wang, G.; Wu, G.; Li, Y. Unveiling Active Sites of CO₂ Reduction on Nitrogen-Coordinated and Atomically Dispersed Iron and Cobalt Catalysts. *ACS Catal.* **2018**, *8*, 3116–3122.
- (21) Hu, X.-M.; Hval, H. H.; Bjerglund, E. T.; Dalgaard, K. J.; Madsen, M. R.; Pohl, M.-M.; Welter, E.; Lamagni, P.; Buhl, K. B.; Bremholm, M.; Beller, M.; Pedersen, S. U.; Skrydstrup, T.; Daasbjerg, K. Selective CO₂ Reduction to CO in Water Using Earth-Abundant Metal and Nitrogen-Doped Carbon Electrocatalysts. *ACS Catal.* **2018**, *8*, 6255–6264.
- (22) Li, J.; Ghoshal, S.; Liang, W.; Sougrati, M.-T.; Jaouen, F.; Halevi, B.; McKinney, S.; McCool, G.; Ma, C.; Yuan, X.; Ma, Z.-F.; Mukerjee, S.; Jia, Q. Structural and Mechanistic Basis for the High Activity of Fe–N–C Catalysts Toward Oxygen Reduction. *Energy Environ. Sci.* **2016**, *9*, 2418–2432.
- (23) Proietti, E.; Jaouen, F.; Lefèvre, M.; Larouche, N.; Tian, J.; Herranz, J.; Dodelet, J.-P. Iron-based cathode catalyst with enhanced power density in polymer electrolyte membrane fuel cells. *Nat. Commun.* **2011**, *2*, 416.
- (24) Zitolo, A.; Ranjbar-Sahraie, N.; Mineva, T.; Li, J.; Jia, Q.; Stamatina, S.; Harrington, G. F.; Lyth, S. M.; Krttil, P.; Mukerjee, S.; Fonda, E.; Jaouen, F. Identification of Catalytic Sites in Cobalt-Nitrogen-Carbon Materials for the Oxygen Reduction Reaction. *Nat. Commun.* **2017**, *8*, 957.
- (25) Zitolo, A.; Goellner, V.; Armel, V.; Sougrati, M.-T.; Mineva, T.; Stievano, L.; Fonda, E.; Jaouen, F. Identification of Catalytic Sites for Oxygen Reduction in Iron- and Nitrogen-Doped Graphene Materials. *Nat. Mater.* **2015**, *14*, 937–942.
- (26) Kramm, U. I.; Lefèvre, M.; Larouche, N.; Schmeisser, D.; Dodelet, J.-P. Correlations Between Mass Activity and Physicochemical Properties of Fe/N/C Catalysts for the ORR in PEM Fuel Cell via ⁵⁷Fe Mossbauer Spectroscopy and Other Techniques. *J. Am. Chem. Soc.* **2014**, *136*, 978–985.
- (27) Xia, Z.; An, L.; Chen, P.; Xia, D. Non-Pt Nanostructured Catalysts for Oxygen Reduction Reaction: Synthesis, Catalytic Activity and Its Key Factors. *Adv. Energy Mater.* **2016**, *6*, 1600458.
- (28) Gewirth, A. A.; Varnell, J. A.; DiAscro, A. M. Nonprecious Metal Catalysts for Oxygen Reduction in Heterogeneous Aqueous Systems. *Chem. Rev.* **2018**, *118*, 2313–2339.
- (29) Jiang, H.; Lin, Y.; Chen, B.; Zhang, Y.; Liu, H.; Duan, X.; Chen, D.; Song, L. Ternary Interfacial Superstructure Enabling Extraordinary Hydrogen Evolution Electrocatalysis. *Mater. Today* **2018**, *21*, 602–610.
- (30) Jin, Q.; Ren, B.; Li, D.; Cui, H.; Wang, C. In Situ Promoting Water Dissociation Kinetic of Co Based Electrocatalyst for Unprecedentedly Enhanced Hydrogen Evolution Reaction in Alkaline Media. *Nano Energy* **2018**, *49*, 14–22.
- (31) Fan, X.; Peng, Z.; Ye, R.; Zhou, H.; Guo, X. M₃C (M: Fe, Co, Ni) Nanocrystals Encased in Graphene Nanoribbons: An Active and Atable Bifunctional Electrocatalyst for Oxygen Reduction and Hydrogen Evolution Reactions. *ACS Nano* **2015**, *9*, 7407–7418.
- (32) Tripkovic, V.; Vanin, M.; Karamad, M.; Björketun, M. E.; Jacobsen, K. W.; Thygesen, K. S.; Rossmeisl, J. Electrochemical CO₂ and CO Reduction on Metal-Functionalized Porphyrin-Like Graphene. *J. Phys. Chem. C* **2013**, *117*, 9187–9195.
- (33) Bagger, A.; Ju, W.; Varela, A. S.; Strasser, P.; Rossmeisl, J. Single Site Porphyrine-Like Structures Advantages Over Metals for Selective Electrochemical CO₂ Reduction. *Catal. Today* **2017**, *288*, 74–78.
- (34) Chan, Y.-T.; Tsai, M.-K. CO₂ Reduction Catalysis by Tunable Square-Planar Transition-Metal Complexes: A Theoretical Investigation Using Nitrogen-Substituted Carbon Nanotube Models. *Phys. Chem. Chem. Phys.* **2017**, *19*, 29068–29076.
- (35) Zhao, Y.; Liang, J.; Wang, C.; Ma, J.; Wallace, G. G. Tunable and Efficient Tin Modified Nitrogen-Doped Carbon Nanofibers for Electrochemical Reduction of Aqueous Carbon Dioxide. *Adv. Energy Mater.* **2018**, *8*, 1702524.
- (36) Zhang, C.; Sha, J.; Fei, H.; Liu, M.; Yazdi, S.; Zhang, J.; Zhong, Q.; Zou, X.; Zhao, N.; Yu, H.; Jiang, Z.; Ringe, E.; Jakobson, B. I.; Dong, J.; Chen, D.; Tour, J. M. Single-Atomic Ruthenium Catalytic Sites on Nitrogen-Doped Graphene for Oxygen Reduction Reaction in Acidic Medium. *ACS Nano* **2017**, *11*, 6930–6941.
- (37) Wei, S.; Li, A.; Liu, J.-C.; Li, Z.; Chen, W.; Gong, Y.; Zhang, Q.; Cheong, W.-C.; Wang, Y.; Zheng, L.; Xiao, H.; Chen, C.; Wang, D.; Peng, Q.; Gu, L.; Han, X.; Li, J.; Li, Y. Direct Observation of Noble Metal Nanoparticles Transforming to Thermally Stable Single Atoms. *Nat. Nanotechnol.* **2018**, *13*, 856–861.
- (38) Cheng, Y.; Zhao, S.; Johannessen, B.; Veder, J.-P.; Saunders, M.; Rowles, M. R.; Cheng, M.; Liu, C.; Chisholm, M. F.; De Marco, R.; Cheng, H.-M.; Yang, S.-Z.; Jiang, S. P. Atomically Dispersed Transition Metals on Carbon Nanotubes with Ultrahigh Loading for Selective Electrochemical Carbon Dioxide Reduction. *Adv. Mater.* **2018**, *30*, 1706287.
- (39) Artyushkova, K.; Matanovic, I.; Halevi, B.; Atanassov, P. Oxygen Binding to Active Sites of Fe–N–C ORR Electrocatalysts Observed by Ambient-Pressure XPS. *J. Phys. Chem. C* **2017**, *121*, 2836–2843.
- (40) Gupta, N.; Gattrell, M.; MacDougall, B. Calculation for the Cathode Surface Concentrations in the Electrochemical Reduction of CO₂ in KHCO₃ solutions. *J. Appl. Electrochem.* **2006**, *36*, 161–172.
- (41) Kresse, G.; Furthmüller, J. Efficiency of Ab-Initio Total Energy Calculations for Metals and Semiconductors Using a Plane-Wave Basis Set. *Comput. Mater. Sci.* **1996**, *6*, 15–50.
- (42) Kresse, G.; Joubert, D. From Ultrasoft Pseudopotentials to the Projector Augmented-Wave Method. *Phys. Rev. B: Condens. Matter Mater. Phys.* **1999**, *59*, 1758–1775.
- (43) Grimme, S.; Antony, J.; Ehrlich, S.; Krieg, H. A Consistent and Accurate Ab Initio Parametrization of Density Functional Dispersion Correction (DFT-D) for the 94 Elements H–Pu. *J. Chem. Phys.* **2010**, *132*, 154104.
- (44) Perdew, J. P.; Burke, K.; Ernzerhof, M. Generalized Gradient Approximation Made Simple. *Phys. Rev. Lett.* **1996**, *77*, 3865–3868.
- (45) Blöchl, P. E. Projector Augmented-Wave Method. *Phys. Rev. B: Condens. Matter Mater. Phys.* **1994**, *50*, 17953–17979.
- (46) Greenwood, N. N.; Earnshaw, A. *Chemistry of the Elements*; Elsevier: Oxford, 2012.
- (47) Monkhorst, H. J.; Pack, J. D. Special Points for Brillouin-Zone Integrations. *Phys. Rev. B: Solid State* **1976**, *13*, 5188–5192.
- (48) Peterson, A. A.; Abild-Pedersen, F.; Studt, F.; Rossmeisl, J.; Nørskov, J. K. How Copper Catalyzes the Electroreduction of Carbon Dioxide into Hydrocarbon Fuels. *Energy Environ. Sci.* **2010**, *3*, 1311–1315.
- (49) Nørskov, J. K.; Rossmeisl, J.; Logadóttir, A.; Lindqvist, L.; Kitchin, J. R.; Bligaard, T.; Jónsson, H. Origin of the Overpotential for Oxygen Reduction at a Fuel-Cell Cathode. *J. Phys. Chem. B* **2004**, *108*, 17886–17892.
- (50) Togo, A.; Tanaka, I. First Principles Phonon Calculations in Materials Science. *Scr. Mater.* **2015**, *108*, 1–5.

- (51) Álvarez-Moreno, M.; de Graaf, C.; Lopez, N.; Maseras, F.; Poblet, J. M.; Bo, C. Managing the Computational Chemistry Big Data Problem: the ioChem-BD Platform. *J. Chem. Inf. Model.* **2015**, *55*, 95–103.
- (52) Pršlja, P. <https://doi.org/10.19061/iochem-bd-1-115> (accessed Jun 14, 2019).
- (53) Zagal, J. H.; Koper, M. T. M. Reactivity Descriptors for the Activity of Molecular MN_4 Catalysts for the Oxygen Reduction Reaction. *Angew. Chem., Int. Ed.* **2016**, *55*, 14510–14521.
- (54) Lefèvre, M.; Dodelet, J. P.; Bertrand, P. Molecular Oxygen Reduction in PEM Fuel Cell Conditions: ToF-SIMS Analysis of Co-Based Electrocatalysts. *J. Phys. Chem. B* **2005**, *109*, 16718–16724.
- (55) Lalonde, G.; Cote, R.; Guay, D.; Dodelet, J. P.; Weng, L. T.; Bertrand, P. Is Nitrogen Important in the Formulation of Fe-based Catalysts for Oxygen Reduction in Solid Polymer Fuel Cells? *Electrochim. Acta* **1997**, *42*, 1379–1388.
- (56) Xu, H.; Cheng, D.; Cao, D.; Zeng, X. C. A Universal Principle for a Rational Design of Single-Atom Electrocatalysts. *Nat. Catal.* **2018**, *1*, 339.
- (57) Grosvenor, A. P.; Kobe, B. A.; Biesinger, M. C.; McIntyre, N. S. Investigation of Multiplet Splitting of Fe 2p XPS Spectra and Bonding in Iron Compounds. *Surf. Interface Anal.* **2004**, *36*, 1564–1574.
- (58) Kuang, M.; Tao Li, T.; Chen, H.; Mao Zhang, S.; Li Zhang, L.; Xin Zhang, Y. Hierarchical $Cu_2O/CuO/Co_3O_4$ Core-Shell Nanowires: Synthesis and Electrochemical Properties. *Nanotechnology* **2015**, *26*, 304002–304011.
- (59) Weidler, N.; Schuch, J.; Knaus, F.; Stenner, P.; Hoch, S.; Maljusch, A.; Schäfer, R.; Kaiser, B.; Jaegermann, W. X-ray Photoelectron Spectroscopic Investigation of Plasma-Enhanced Chemical Vapor Deposited NiO_x , $NiO_x(OH)_y$, and $CoNiO_x(OH)_y$: Influence of the Chemical Composition on the Catalytic Activity for the Oxygen Evolution Reaction. *J. Phys. Chem. C* **2017**, *121*, 6455–6463.
- (60) Pervaiz, E.; Tareen, A. K.; Yang, M. Bimetallic Oxide Nanoflowers Decorated Graphene Oxide Nanosheets as Novel Nanohybrids for 4-Nitrophenol Removal at Room Temperature. *Nanoscale Adv.* **2017**, *2*, 1–7.
- (61) Jeon, H. S.; Ahn, S. J.; Jee, M. S.; Yoon, S. S.; Hwang, Y. J.; Min, B. K. Water Oxidation by Manganese Oxide Electrocatalytic Films Synthesized by Chemical Solution Deposition Method. *J. Electrochem. Soc.* **2016**, *163*, F3113–F3118.
- (62) Kattel, S.; Atanassov, P.; Kiefer, B. Catalytic Activity of $Co-N_x/C$ Electrocatalysts for Oxygen Reduction Reaction: A Density Functional Theory Study. *Phys. Chem. Chem. Phys.* **2013**, *15*, 148–153.
- (63) Kattel, S.; Atanassov, P.; Kiefer, B. Stability, Electronic and Magnetic Properties of In-Plane Defects in Graphene: A First-Principles Study. *J. Phys. Chem. C* **2012**, *116*, 8161–8166.
- (64) Lefèvre, M.; Proietti, E.; Jaouen, F.; Dodelet, J.-P. Iron-Based Catalysts with Improved Oxygen Reduction Activity in Polymer Electrolyte Fuel Cells. *Science* **2009**, *324*, 71–74.
- (65) Jaouen, F.; Lefèvre, M.; Dodelet, J.-P.; Cai, M. Heat-Treated Fe/N/C Catalysts for O_2 Electroreduction: Are Active Sites Hosted in Micropores? *J. Phys. Chem. B* **2006**, *110*, 5553–5558.
- (66) Varela, A. S.; Ranjbar Sahraie, N.; Steinberg, J.; Ju, W.; Oh, H.-S.; Strasser, P. Metal-Doped Nitrogenated Carbon as an Efficient Catalyst for Direct CO_2 Electroreduction to CO and Hydrocarbons. *Angew. Chem., Int. Ed.* **2015**, *54*, 10758–10762.
- (67) Leonard, N.; Ju, W.; Sinev, I.; Steinberg, J.; Luo, F.; Varela, A. S.; Roldan Cuenya, B.; Strasser, P. The Chemical Identity, State and Structure of Catalytically Active Centers During the Electrochemical CO_2 Reduction on Porous Fe–Nitrogen–Carbon (Fe–N–C) Materials. *Chem. Sci.* **2018**, *9*, 5064–5073.
- (68) Pan, Y.; Lin, R.; Chen, Y.; Liu, S.; Zhu, W.; Cao, X.; Chen, W.; Wu, K.; Cheong, W.-C.; Wang, Y.; Zheng, L.; Luo, J.; Lin, Y.; Liu, Y.; Liu, C.; Li, J.; Lu, Q.; Chen, X.; Wang, D.; Peng, Q.; Chen, C.; Li, Y. Design of Single-Atom Co– N_5 Catalytic Site: A Robust Electrocatalyst for CO_2 Reduction with nearly 100% CO Selectivity and Remarkable Stability. *J. Am. Chem. Soc.* **2018**, *140*, 4218–4221.
- (69) Wang, X.; Chen, Z.; Zhao, X.; Yao, T.; Chen, W.; You, R.; Zhao, C.; Wu, G.; Wang, J.; Huang, W.; Yang, J.; Hong, X.; Wei, S.; Wu, Y.; Li, Y. Regulation of Coordination Number Over Single Co Sites: Triggering the Efficient Electroreduction of CO_2 . *Angew. Chem.* **2018**, *130*, 1962–1966.
- (70) Göttle, A. J.; Koper, M. T. M. Determinant Role of Electrogenerated Reactive Nucleophilic Species on Selectivity During Reduction of CO_2 Catalyzed by Metalloporphyrins. *J. Am. Chem. Soc.* **2018**, *140*, 4826–4834.
- (71) Wang, R.; Sun, X.; Ould-Chikh, S.; Osadchii, D.; Bai, F.; Kapteijn, F.; Gascon, J. Metal-Organic-Framework-Mediated Nitrogen-Doped Carbon for CO_2 Electrochemical Reduction. *ACS Appl. Mater. Interfaces* **2018**, *10*, 14751–14758.
- (72) Siahrostami, S.; Jiang, K.; Karamad, M.; Chan, K.; Wang, H.; Nørskov, J. Theoretical Investigations into Defected Graphene for Electrochemical Reduction of CO_2 . *ACS Sustainable Chem. Eng.* **2017**, *5*, 11080–11085.
- (73) Weng, Z.; Wu, Y.; Wang, M.; Jiang, J.; Yang, K.; Huo, S.; Wang, X.-F.; Ma, Q.; Brudvig, G. W.; Batista, V. S.; Liang, Y.; Feng, Z.; Wang, H. Active Sites of Copper-Complex Catalytic Materials for Electrochemical Carbon Dioxide Reduction. *Nat. Commun.* **2018**, *9*, 415.
- (74) Li, J.; Alsudairi, A.; Ma, Z.-F.; Mukerjee, S.; Jia, Q. Asymmetric Volcano Trend in Oxygen Reduction Activity of Pt and Non-Pt Catalysts: In Situ Identification of the Site-Blocking Effect. *J. Am. Chem. Soc.* **2017**, *139*, 1384–1387.
- (75) Fletcher, S. Tafel Slopes from First Principles. *J. Solid State Electrochem.* **2009**, *13*, 537–549.
- (76) Stamenkovic, V. R.; Mun, B. S.; Arenz, M.; Mayrhofer, K. J. J.; Lucas, C. A.; Wang, G.; Ross, P. N.; Markovic, N. M. Trends in Electrocatalysis on Extended and Nanoscale Pt-Bimetallic Alloy Surfaces. *Nat. Mater.* **2007**, *6*, 241–247.
- (77) Stamenkovic, V.; Mun, B. S.; Mayrhofer, K. J. J.; Ross, P. N.; Markovic, N. M.; Rossmeisl, J.; Greeley, J.; Nørskov, J. K. Changing the activity of electrocatalysts for oxygen reduction by tuning the surface electronic structure. *Angew. Chem.* **2006**, *118*, 2963–2967.
- (78) Hursán, D.; Samu, A. A.; Janovák, L.; Artyushkova, K.; Asset, T.; Atanassov, P.; Janáky, C. Morphological Attributes Govern Carbon Dioxide Reduction on N-Doped Carbon Electrodes. *Joule* **2019**, *3*, 1719–1733.